3

Distributed-Parameter Modeling of Energy Harvesting Structures with Discontinuities

Adam Wickenheiser
George Washington University, United States

1. Introduction

Energy harvesting – the ability to gather energy from the local environment to power wireless devices – has seen significant development over the past decade as the demand for portable electronics increases. Although on-board batteries provide a simple means of providing energy for these devices, their energy density can be insufficient for miniature devices or long-term deployment (Anton & Sodano, 2007). A means of replenishing on-board energy storage has the potential to reduce the frequency of battery replacement or eliminate the need altogether. Vibration-based energy harvesting in particular has garnered much attention due to the ubiquity of vibrational energy in the environment (Roundy et al., 2003). Several methods of electromechanical transduction from vibrations have been investigated, including electromagnetic induction, electrostatic varactance, and the piezoelectric effect, the latter being the province of this chapter.

Mechanical energy is transformed into electricity by straining piezoelectric material mounted on a structure that is subjected to ambient vibrations. If a natural frequency of the structure is matched to the predominant excitation frequency, resonance occurs, where large strains are induced by relatively small excitations. A major problem with resonant vibration-based energy harvesters is that their peak strain (and hence, power) only occurs near the natural frequencies of the transducer. For many potential applications, ambient vibrations are low frequency, requiring large or heavy structures for resonance (Roundy et al., 2003; Wickenheiser & Garcia, 2010a). In order to shrink the size and mass of these devices while reducing their natural frequencies, a variety of techniques have been employed. For example, changing the standard cantilevered beam geometry and manipulating the mass distribution along the beam have been investigated. Varying the cross sections along the beam length (Dietl & Garcia, 2010; Reissman et al., 2007; Roundy et al., 2005) and the ratio of tip mass to beam mass (Dietl & Garcia, 2010; Wickenheiser, 2011) have been shown to improve the electromechanical coupling (a factor in the energy conversion rate) over a uniform cantilever beam design. Changing the number and location of piezoelectric patches or layers along the beam can improve coupling and shift the natural frequency of the device (Guyomar et al., 2005; Wu et al., 2009). Multi-beam structures can compact the design by folding it in on itself while retaining a similar natural frequency to the original, straight configuration (Karami & Inman, 2011; Erturk et al., 2009). A nonlinear technique called "frequency up-conversion" also shows promise to boost power at frequencies more than an order of magnitude below resonance (Murray & Rastegar, 2009; Tieck et al., 2006;

Wickenheiser & Garcia, 2010b). Despite the prevalence of widely varying designs, no single analytic method exists for predicting the electromechanical behavior of these systems.

In the energy harvesting literature, the piezoelectric transducer is commonly modeled as a lumped, single-degree-of-freedom (DOF) system, typically a current source in parallel with an intrinsic capacitance. To more accurately predict the dynamics of energy harvesters, mechanical models have been developed based on their geometry and material properties. Two common approaches to modeling and simulating these devices are lumped parameter (typically single DOF) (duToit et al., 2005; Roundy & Wright, 2004) and distributed parameter (multi-DOF) (duToit et al., Erturk & Inman, 2008; Sodano et al., 2004; Wickenheiser & Garcia, 2010c) models. Lumped parameter models are simple and accurate when vibrating near a resonant frequency and experimental data are available to estimate the model parameters. Distributed parameter models are more accurate when multiple modes of vibration are expressed, can predict geometric effects such as charge cancellation, and can be easily extended to include arbitrary DOFs. However, these models are much more complex, are designed for a specific geometry, and require experimental determination of some of their parameters.

In this chapter, a straightforward analytic approach is taken for modeling beams of varying cross-sectional geometry and multiple discontinuities, including lumped masses and bends. This technique also correctly accounts for the changes in the mechanical response from adding piezoelectric layers with partial coverage to the structure. This method is derived from the classical transfer matrix method (TMM) for multi-component structures and trusses (Pestel & Leckie, 1963) combined with an existing model for constant cross section, Euler-Bernoulli beam energy harvesters (Wickenheiser & Garcia, 2010c). A variation of this technique is employed by (Karami & Inman, 2011) to find the natural frequencies and mode shapes of a zigzag structure; however, their formulation is specific to 180° bends between segments. The TMM has been shown to reduce to the classical solutions (e.g. cantilevered beam with or without tip mass) for structures consisting of a single segment (Reissman et al., 2011). An advantage of this method is that increasing the complexity of the structure does not increase the size of the eigenvalue problem required to find the natural frequencies and mode shapes. Furthermore, the same formulation can be used for an arbitrary distribution of lumped masses, bends between members, and varying geometry beam segments.

In the following sections, the equations of motion (EOMs) are derived for uniform beam segments and for lumped masses. Subsequently, it is shown how these subsystems can be combined to form an arbitrarily complex structure. The eigenvalue problem for this class of design is then solved for the natural frequencies and mode shapes. These solutions are incorporated into a partial differential equation (PDE) model that includes the linearized piezoelectric constitutive equations, enabling the solution of the coupled electromechanical dynamics. Finally, a few simple case studies are presented to highlight the usefulness of this technique.

2. Derivation of TMM for Euler-Bernoulli beam structures

2.1 Overview of methodology

The transfer matrix method used in this study is derived from the methodology described in (Pestel & Leckie, 1963). This method is used to calculate the natural frequencies and mode shapes (i.e. the eigensolution) for piecewise continuous structures, such as the one shown in

Fig. 1. This figure shows a 3-segment beam with lumped masses connected to the tip of each segment. (In this discussion, the "base" of each segment is the end closest to the host structure, whereas the "tip" is the end furthest.) Each segment is assumed to have constant geometric and material properties; however, different segments may have different properties. The lumped masses and bend angles can vary for each segment, including the case of no lumped mass between two segments. Furthermore, each segment may have a different number and arrangement of piezoelectric and substructure layering – e.g. combining bimorph, unimorph, and bare substructure.

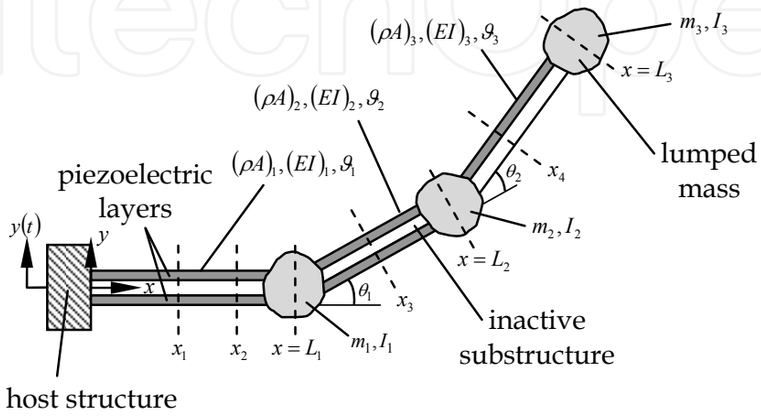

Fig. 1. Layout and geometric parameters of an example piecewise continuous structure.

Let $w(x,t)$ be the deflection of the beam in the transverse direction and $u(x,t)$ be the deflection in the axial direction, each measured relative to the equilibrium position of the structure. Separation of variables is adopted to decompose these deflections into spatial and temporal components:

$$w(x,t) = \sum_{r=1}^{\infty} \eta_r(t)\phi_r(x) \text{ and } u(x,t) = \sum_{r=1}^{\infty} \eta_r(t)\psi_r(x) \tag{1}$$

where $\eta_r(t)$ is the r^{th} modal displacement, $\phi_r(x)$ is the r^{th} transverse mode shape function, and $\psi_r(x)$ is the r^{th} axial mode shape function. The subscript r is henceforth dropped for clarity, since the following discussion applies to any mode.

As will be discussed in the following sections, Euler-Bernoulli beam theory requires 4 states to describe the variation of ϕ with respect to x, namely the mode shape itself ϕ, its slope $d\phi/dx$, the internal bending moment M, and the internal shear force V. The state equation for the variation of ψ with respect to x includes the mode shape itself ψ and the normal (i.e. axial force) N. Assembling these variables into a state vector

$$\mathbf{z} = \begin{bmatrix} \psi & N & \phi & \dfrac{d\phi}{dx} & M & V \end{bmatrix}^T \tag{2}$$

a 6x6 linear system of the form

$$\frac{d\mathbf{z}}{dx} = \mathbf{A}(x)\mathbf{z}(x) \tag{3}$$

will be derived subsequently. Using the state transition matrix $\mathbf{\Phi}$ of Eq. (3), the state vectors at any two points along the structure can be related using

$$\mathbf{z}(x_2) = \mathbf{\Phi}(x_2, x_1)\mathbf{z}(x_1) \tag{4}$$

At this stage, the power of the transfer matrix method becomes apparent. Consider the problem of relating the states (components of $\mathbf{z}$) between points x_1 and x_2 and between points x_3 and x_4 shown in Fig. 1. In the next sections, state transition matrices will be derived for each beam segment, called *field transfer matrices*, and each lumped mass, called *point transfer matrices*. Denoting the field transfer matrix for the j^{th} segment $\mathbf{F_j}$ and the point transfer matrix for the j^{th} lumped mass $\mathbf{P_j}$, it will be shown that Eq. (4) can be written as

$$\mathbf{z}(x_2) = \mathbf{F_1}(x_2 - x_1)\mathbf{z}(x_1) \tag{5a}$$

between points x_1 and x_2 and

$$\mathbf{z}(x_4) = \mathbf{F_3}(x_4 - L_2)\mathbf{P_2}\mathbf{F_2}(L_2 - x_3)\mathbf{z}(x_3) \tag{5b}$$

between points x_3 and x_4, using the semigroup property of state transition matrices. Eq. (5b) also displays another feature of the transfer matrix method: no matter how many beam segments and lumped masses there are in the structure, the problem never grows beyond a 6x6 linear system.

2.2 Derivation of EOMs for an Euler-Bernoulli beam segment

In this section, the EOMs for the states across a uniform beam segment are derived using Euler-Bernoulli beam assumptions and linearized material constitutive equations. The approach taken herein is based on force and moment balances and is a generalization of the treatments by (Erturk & Inman, 2008; Söderkvist, 1990; Wickenheiser & Garcia, 2010c). It is assumed that each beam segment is uniform in cross section and material properties. Furthermore, the standard Euler-Bernoulli beam assumptions are adopted, including negligible rotary inertia and shear deformation (Inman, 2007).

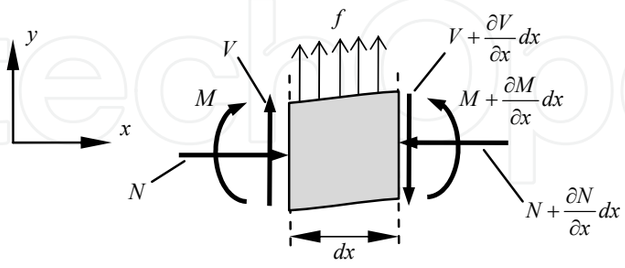

Fig. 2. Free-body diagram of Euler-Bernoulli beam segment

Consider the free-body diagram shown in Fig. 2. Dropping higher order terms, balances of forces in the *y*-direction and moments yield

$$\frac{\partial V(x,t)}{\partial x} + f(x,t) = (\rho A)\frac{\partial^2 w(x,t)}{\partial t^2} \tag{6a}$$

$$\frac{\partial M(x,t)}{\partial x} = -V(x,t) \tag{6b}$$

where $V(x,t)$ is the shear force, $M(x,t)$ is the internal moment generated by mechanical and electrical strain, $f(x,t)$ is the externally applied force per unit length (it will be shown later that this is the inertial force induced by the base excitation), and (ρA) is the mass per unit length (Inman, 2007). Note that if the segment is monolithic, (ρA) is simply the product of the density of the material and the cross-sectional area. For the case of a bimorph beam segment, this term is given by

$$(\rho A) = \frac{m}{l} = \frac{\rho_s t_s bl + 2\rho_p t_p bl}{l} = b\left(\rho_s t_s + 2\rho_p t_p\right) \tag{7}$$

The internal bending moment is the net contribution of the stresses in the axial direction in the beam. The stress within the piezoelectric layers is found from the linearized constitutive equations

$$\begin{aligned} T_1 &= c_{11}^E S_1 - e_{31} E_3 \\ D_3 &= e_{31} S_1 + \varepsilon_{33}^S E_3 \end{aligned} \tag{8}$$

where T is stress, S is strain, E is electric field, D is electric displacement, c is Young's Modulus, e is piezoelectric constant, and ε is dielectric constant. The subscripts indicate the direction of perturbation; in the cantilever configuration shown in Fig. 1, 1 corresponds to axial and 3 corresponds to transverse. The superscript $(\cdot)^E$ indicates a linearization at constant electric field, and the superscript $(\cdot)^S$ indicates a linearization at constant strain (IEEE, 1987). The stress within the substrate layer(s) is given simply by the linear stress-strain relationship $T_1 = c_{11,s} S_1$, where $c_{11,s}$ is Young's Modulus of the substrate material in the axial direction. Since deformations are assumed small, the axial strain is the same as the case of pure bending, which is given by $S_1 = -y\,\partial^2 w(x,t)/\partial x^2$ (Beer & Johnson, 1992), and the transverse electric field is assumed constant and equal to $E_3 = \pm v(t)/t_p$, where $v(t)$ is the voltage across the electrodes, and the top and bottom layer have opposite signs due to the parallel configuration wiring. (This approximation is reasonable given the thinness of the layers.) Consider the case of a bimorph beam segment of width b, substrate layer thickness t_s, and piezoelectric layer thickness t_p. Then the bending moment is

$$\begin{aligned} M(x,t) = & \int_{-t_s/2-t_p}^{-t_s/2} T_1 by\,dy + \int_{-t_s/2}^{t_s/2} T_1 by\,dy + \int_{t_s/2}^{t_s/2+t_p} T_1 by\,dy \\ = & -\left[\int_{-t_s/2-t_p}^{-t_s/2} c_{11}^E by^2\,dy + \int_{-t_s/2}^{t_s/2} c_{11,s} by^2\,dy + \int_{t_s/2}^{t_s/2+t_p} c_{11}^E by^2\,dy\right]\frac{\partial^2 w(x,t)}{\partial x^2} \\ & -\left[\int_{-t_s/2-t_p}^{-t_s/2} \frac{e_{31}}{t_p} by\,dy - \int_{t_s/2}^{t_s/2+t_p} \frac{e_{31}}{t_p} by\,dy\right] v(t)\left[H(x-L_L) - H(x-L_R)\right] \\ = & \underbrace{\left\{c_{11,s} b\frac{t_s^3}{12} + 2c_{11}^E b\left[\frac{t_p^3}{12} + t_p\left(\frac{t_p+t_s}{2}\right)^2\right]\right\}}_{(EI)}\frac{\partial^2 w(x,t)}{\partial x^2} + \underbrace{-e_{31} b\left(t_s+t_p\right)}_{\vartheta} v(t)\left[H(x-L_L) - H(x-L_R)\right] \end{aligned} \tag{9}$$

where $H(\cdot)$ is the Heaviside step function, and L_L, L_R are the left and right ends of the segment, respectively. In Eq. (9), the constant multiplying the $\partial^2 w(x,t)/\partial x^2$ term is defined as (EI), the effective bending stiffness. (Note that if the beam segment is monolithic, this constant is simply the product of the Young's Modulus and the moment of inertia.) The constant multiplying the $v(t)$ term is defined as ϑ, the electromechanical coupling coefficient. Substituting Eq. (9) into Eq. (6) yields

$$(\rho A)\frac{\partial^2 w(x,t)}{\partial t^2} + (EI)\frac{\partial^4 w(x,t)}{\partial x^4} + \vartheta\left[\frac{d\delta(x-L_L)}{dx} - \frac{d\delta(x-L_R)}{dx}\right]v(t) = f(x,t) \tag{10}$$

which is the transverse mechanical EOM for a beam segment.

The electrical EOM can be found by integrating the electric displacement over the surface of the electrodes, yielding the net charge $q(t)$ (IEEE, 1987):

$$\begin{aligned} q(t) &= \iint_{\substack{\text{upper}\\\text{layer}}} D_3 dA - \iint_{\substack{\text{lower}\\\text{layer}}} D_3 dA \\ &= b\int_{L_L}^{L_R}\left[\frac{1}{t_p}\int_{t_s/2}^{t_s/2+t_p} -e_{31} y\frac{\partial^2 w(x,t)}{\partial x^2}dy - \frac{\varepsilon_{33}^S}{t_p}v(t)\right]dx \\ &\quad -b\int_{L_L}^{L_R}\left[\frac{1}{t_p}\int_{-t_s/2-t_p}^{-t_s/2} -e_{31} y\frac{\partial^2 w(x,t)}{\partial x^2}dy + \frac{\varepsilon_{33}^S}{t_p}v(t)\right]dx \\ &= \underbrace{-e_{31}b\left(t_s+t_p\right)}_{\vartheta}\left[\left.\frac{\partial w(x,t)}{\partial x}\right|_{x=L_R} - \left.\frac{\partial w(x,t)}{\partial x}\right|_{x=L_L}\right] - \underbrace{\frac{2\varepsilon_{33}^S bL}{t_p}}_{C}v(t) \end{aligned} \tag{11}$$

where the constant multiplying the $v(t)$ term is defined as C, the net clamped capacitance of the segment. Eqs. (10–11) provide a coupled system of equations; these can be solved by relating the voltage $v(t)$ to the charge $q(t)$ through the external electronic interface.

To derive the EOMs for the axial motion of each segment, it is assumed that the deformations in this direction are negligible compared to the transverse deformations. This assumption is reasonable if the cross sections are very thin in the transverse direction, in which case $A >> I$. Thus, if the beam is assumed rigid in the *x*-direction, a balance of forces gives

$$(\rho A)\frac{\partial^2 u(x,t)}{\partial t^2} + \frac{\partial N(x,t)}{\partial x} = 0 \tag{12}$$

which constitutes the EOM for the axial direction for each beam segment. It should be noted that in Eqs. (10–12), the constants in the equations have been derived for bimorph segments; constants for other configurations can be found in (Wickenheiser & Garcia, 2010c). These three equations are the EOMs for this structure, which are solved in Section 4.

2.3 Field transfer matrix derivation

To derive the state transition matrix between two points along a uniform beam segment, the Euler-Bernoulli EOMs derived in the previous section are employed, dropping the

electromechanical coupling effects and the inertial forces due to base excitation, i.e. setting $v(t) \equiv 0$ and $f(x,t) \equiv 0$. This is equivalent to the assumption of Euler-Bernoulli mode shapes when modeling piezoelectric benders, a prevalent simplification appearing in the literature (duToit et al., 2005; Erturk & Inman, 2008; Wickenheiser & Garcia, 2010c). Under these assumptions, Eqs. (6,9,12) become

$$\frac{\partial V(x,t)}{\partial x} = (\rho A)_j \frac{\partial^2 w(x,t)}{\partial t^2}, \; \frac{\partial M(x,t)}{\partial x} = -V(x,t),$$
$$(\rho A)_j \frac{\partial^2 u(x,t)}{\partial t^2} + \frac{\partial N(x,t)}{\partial x} = 0 \text{ and } M(x,t) = (EI)_j \frac{\partial^2 w(x,t)}{\partial x^2} \tag{13}$$

for beam segment *j*.

At this point, Eq. (1) is applied. Each mode shape has a natural frequency ω associated with it (dropping the *r* subscript). With this substitution, the first and third of the previous equations can be rewritten as

$$\frac{dV(x)}{dx} = -(\rho A)_j \omega^2 \phi(x) \text{ and } \frac{dN(x)}{dx} = (\rho A)_j \omega^2 \psi(x) \tag{14}$$

Collecting Eqs. (13–14) and writing them in terms of the mode shapes yields the linear system

$$\frac{d}{dx}\underbrace{\begin{bmatrix} \psi \\ N \\ \phi \\ d\phi/dx \\ M \\ V \end{bmatrix}}_{\mathbf{z}} = \underbrace{\left[\begin{array}{cc|cccc} 0 & 0 & 0 & 0 & 0 & 0 \\ (\rho A)_j \omega^2 & 0 & 0 & 0 & 0 & 0 \\ \hline 0 & 0 & 0 & 1 & 0 & 0 \\ 0 & 0 & 0 & 0 & \frac{1}{(EI)_j} & 0 \\ 0 & 0 & 0 & 0 & 0 & -1 \\ 0 & 0 & -(\rho A)_j \omega^2 & 0 & 0 & 0 \end{array}\right]}_{\mathbf{A_j}} \underbrace{\begin{bmatrix} \psi \\ N \\ \phi \\ d\phi/dx \\ M \\ V \end{bmatrix}}_{\mathbf{z}} \tag{15}$$

which is the form sought in Eq. (3). Note that the transverse and axial dynamics are decoupled.

Within a beam segment, the cross sections are assumed constant along the length, which has resulted in a constant state matrix $\mathbf{A_j}$ in Eq. (15). Hence, from linear systems theory, the state transition matrix is simply a function of the *difference* in the positions along the beam, i.e. $\mathbf{\Phi}(x_2, x_1) = \mathbf{\Phi}(x_2 - x_1) \equiv \mathbf{\Phi}(\Delta x)$. Thus, the field transfer matrix for beam segment *j* can be written as $\mathbf{F_j}(\Delta x) = e^{\mathbf{A_j}\Delta x}$.

Since $\mathbf{A_j}$ is block diagonal, the matrix exponential can be computed for each block separately. The upper left block can be integrated explicitly. An analytical formula for the matrix exponential of the lower-right block, labeled $\mathbf{B_j}$, can be found using the Cayley-Hamilton theorem, which states

$$e^{\mathbf{B_j}\Delta x} = c_0 I + c_1\left(\mathbf{B_j}\Delta x\right) + c_2\left(\mathbf{B_j}\Delta x\right)^2 + c_3\left(\mathbf{B_j}\Delta x\right)^3 \tag{16}$$

This equation must hold when $\mathbf{B_j}$ is replaced by any of its eigenvalues, which are given by $\lambda = \pm\beta$ and $\lambda = \pm i\beta$, where

$$\beta^4 = \frac{(\rho A)_j\,\omega^2}{(EI)_j} \tag{17}$$

Substituting these eigenvalues into Eq. (16) yields a system of 4 equations for the unknowns $c_0,\ldots,c_3$. The solution of these equations is

$$\begin{aligned}
c_0 &= \frac{1}{2}\left[\cosh(\beta\Delta x) + \cos(\beta\Delta x)\right] \\
c_1 &= \frac{1}{2(\beta\Delta x)}\left[\sinh(\beta\Delta x) + \sin(\beta\Delta x)\right] \\
c_2 &= \frac{1}{2(\beta\Delta x)^2}\left[\cosh(\beta\Delta x) - \cos(\beta\Delta x)\right] \\
c_3 &= \frac{1}{2(\beta\Delta x)^3}\left[\sinh(\beta\Delta x) - \sin(\beta\Delta x)\right]
\end{aligned} \tag{18}$$

Substituting these formulas back into Eq. (16) and concatenating with the upper-left block yields

$$\mathbf{F_j}(\Delta x) = \left[\begin{array}{cc|cccc}
1 & 0 & 0 & 0 & 0 & 0 \\
\Delta x(\rho A)_j\,\omega^2 & 1 & 0 & 0 & 0 & 0 \\
\hline
0 & 0 & c_0 & \Delta x c_1 & \dfrac{(\Delta x)^2}{(EI)_j}c_2 & -\dfrac{(\Delta x)^3}{(EI)_j}c_3 \\
0 & 0 & \dfrac{(\Delta x)^3(\rho A)_j\,\omega^2}{(EI)_j}c_3 & c_0 & \dfrac{\Delta x}{(EI)_j}c_1 & -\dfrac{(\Delta x)^2}{(EI)_j}c_2 \\
0 & 0 & (\Delta x)^2(\rho A)_j\,\omega^2 c_2 & (\Delta x)^3(\rho A)_j\,\omega^2 c_3 & c_0 & -\Delta x c_1 \\
0 & 0 & -\Delta x(\rho A)_j\,\omega^2 c_1 & -(\Delta x)^2(\rho A)_j\,\omega^2 c_2 & -\dfrac{(\Delta x)^3(\rho A)_j\,\omega^2}{(EI)_j}c_3 & c_0
\end{array}\right] \tag{19}$$

Eq. (19) is the field transfer matrix of a beam section for relating the state vectors $\mathbf{z}$ at different positions within a single beam segment. A use of this matrix for that purpose is seen in Eq. (5a).

2.4 Point transfer matrix derivation

The point transition matrix $\mathbf{P}$ is now derived, which accounts for discontinuities between the uniform beam segments. Consider the free-body diagram of the lumped mass shown in Fig. 2. This mass is considered a point mass with mass m_j and rotary inertia I_j, located at $x = L_j$. Since the mass is assumed to be infinitesimal in size, the forces and moments are evaluated at $x = L_j -$ and $x = L_j +$, meaning approaching $x = L_j$ from the left and the right, respectively.

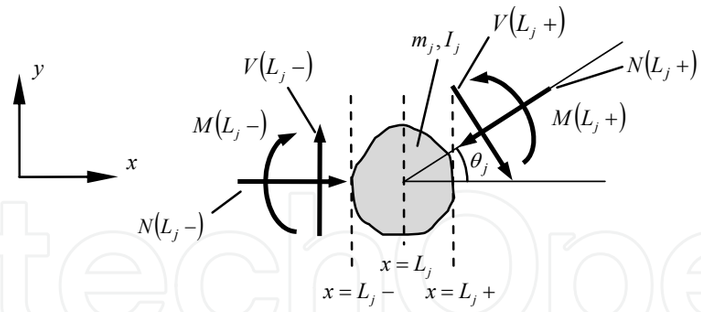

Fig. 3. Forces and moments on a lumped mass located at $x = L_j$.

The slope of the beam is continuous across the lumped mass, hence $d\phi(L_j-)/dx = d\phi(L_j+)/dx$. However, due to the rotation of the local beam coordinate system from one side of the lumped mass to the other, the mode shapes are not continuous, i.e.

$$\begin{bmatrix} \psi(L_j+) \\ \phi(L_j+) \end{bmatrix} = \begin{bmatrix} \cos\theta_j & \sin\theta_j \\ -\sin\theta_j & \cos\theta_j \end{bmatrix} \begin{bmatrix} \psi(L_j-) \\ \phi(L_j-) \end{bmatrix} \tag{20}$$

Furthermore, due to the lumped inertia, the shear force, normal force, and bending moment are not continuous. A balance of forces and moments on the lumped mass, referring to Fig. 3, gives

$$N(L_j+) = (\cos\theta_j)N(L_j-) + (\sin\theta_j)V(L_j-) + (m_j\omega^2\cos\theta_j)\psi(L_j-) + (m_j\omega^2\sin\theta_j)\phi(L_j-) \tag{21}$$

$$V(L_j+) = (-\sin\theta_j)N(L_j-) + (\cos\theta_j)V(L_j-) + (-m_j\omega^2\sin\theta_j)\psi(L_j-) + (m_j\omega^2\cos\theta_j)\phi(L_j-) \tag{22}$$

$$M(L_j+) = -I_j\omega^2\frac{d\phi(L_j-)}{dx} + M(L_j-) \tag{23}$$

Assembling these equations together yields

$$\underbrace{\begin{bmatrix} \psi(L_j+) \\ N(L_j+) \\ \phi(L_j+) \\ d\phi(L_j+)/dx \\ M(L_j+) \\ V(L_j+) \end{bmatrix}}_{\mathbf{z}(L_j+)} = \underbrace{\begin{bmatrix} \cos\theta_j & 0 & \sin\theta_j & 0 & 0 & 0 \\ m_j\omega^2\cos\theta_j & \cos\theta_j & m_j\omega^2\sin\theta_j & 0 & 0 & \sin\theta_j \\ -\sin\theta_j & 0 & \cos\theta_j & 0 & 0 & 0 \\ 0 & 0 & 0 & 1 & 0 & 0 \\ 0 & 0 & 0 & -I_j\omega^2 & 1 & 0 \\ -m_j\omega^2\sin\theta_j & -\sin\theta_j & m_j\omega^2\cos\theta_j & 0 & 0 & \cos\theta_j \end{bmatrix}}_{\mathbf{P_j}} \underbrace{\begin{bmatrix} \psi(L_j-) \\ N(L_j-) \\ \phi(L_j-) \\ d\phi(L_j-)/dx \\ M(L_j-) \\ V(L_j-) \end{bmatrix}}_{\mathbf{z}(L_j-)} \tag{24}$$

which provides a formula for the point transition matrix $\mathbf{P_j}$ of the j^{th} lumped mass. This formula is valid when the lumped mass is at the tip of the structure, in which case $M(L_j+)=V(L_j+)=N(L_j+)=0$ in Eq. (24) (i.e. the free end condition), or if there is no lumped mass between two beam segments, a situation given as a case study below. In this latter case, $m_j=I_j=0$ in Eq. (16). If, furthermore, there is no angle between beam segments, i.e. $\theta_j=0$, then $\mathbf{P_j}$ reduces to the identity matrix, indicating that all of the states are continuous through the junction.

3. Eigensolution using the system transfer matrix

3.1 Natural frequencies

As discussed in section 2.1, the state transition matrix $\mathbf{\Phi}(x_2,x_1)$ relates the states of the system between any points along the beam through Eq. (2). Depending on the locations of x_1 and x_2, the transition matrix is, in general, expressible as a product of field and point transfer matrices, as illustrated by Eqs. (5a–b). The number of matrices in this product is equal to the number of beam segments and junctions between the two points.

It should be noted, though, that at this point the natural frequency ω is still unknown; thus, $\mathbf{\Phi}(x_2,x_1)$ cannot be evaluated between any two points in general. However, the boundary conditions at the ends of the structure provide locations where some of the states are known. In the presently studied cantilever (or "fixed-free") configuration, the following states are known:

$$\psi(0)=\phi(0)=\frac{d\phi}{dx}(0)=0 \text{ and } N(L_n)=M(L_n)=V(L_n)=0 \tag{25}$$

where n is the total number of beam segments. These boundary conditions signify a fixed condition at $x=0$ and a free condition at $x=L_n$. To relate the fixed and free ends, Eq. (4) is employed:

$$\begin{bmatrix} \psi(L_n) \\ N(L_n) \\ \phi(L_n) \\ d\phi(L_n)/dx \\ M(L_n) \\ V(L_n) \end{bmatrix} = \underbrace{\left(\prod_{j=1}^{n} \mathbf{P_{n-j+1}} \mathbf{F_{n-j+1}} \left(L_{n-j+1} - L_{n-j} \right) \right)}_{\mathbf{U}} \begin{bmatrix} \psi(0) \\ N(0) \\ \phi(0) \\ d\phi(0)/dx \\ M(0) \\ V(0) \end{bmatrix} \tag{26}$$

where $\mathbf{U}$, the product of all of the point and field transfer matrices (a result of the semigroup property of $\mathbf{\Phi}$), is called the *system transfer matrix*. This matrix is the state transition matrix from the fixed end to the free end, across all of the beam segments and junctions. As will be demonstrated, this is the matrix that is used in the eigensolution of the structure.

Substituting Eq. (25) into Eq. (26) and examining the 2nd, 5th, and 6th equations of the resulting linear system reveals

$$\begin{bmatrix} 0 \\ 0 \\ 0 \end{bmatrix} = \begin{bmatrix} U_{2,2} & U_{2,5} & U_{2,6} \\ U_{5,2} & U_{5,5} & U_{5,6} \\ U_{6,2} & U_{6,5} & U_{6,6} \end{bmatrix} \begin{bmatrix} N(0) \\ M(0) \\ M(0) \end{bmatrix} \tag{27}$$

where $U_{i,j}$ is the *i,j* component of the system transfer matrix $\mathbf{U}$. Solving the characteristic equation of the matrix appearing in Eq. (27) yields the natural frequencies ω of the structure, and hence, the conditions for the existence of non-trivial solutions to Eq. (27). The resulting characteristic equation is shown to reduce to the standard eigenvalue formulas for cantilevered beams (with or without tip mass) in (Reissman et al., 2011).

3.2 Mode shapes

To compute the mode shapes, Eq. (4) is again revisited, this time evaluated between the fixed end and an arbitrary point along the structure:

$$\begin{bmatrix} \psi(x) \\ N(x) \\ \phi(x) \\ d\phi(x)/dx \\ M(x) \\ V(x) \end{bmatrix} = \mathbf{\Phi}(x,0) \begin{bmatrix} \psi(0) \\ N(0) \\ \phi(0) \\ d\phi(0)/dx \\ M(0) \\ V(0) \end{bmatrix} \tag{28}$$

The first equation in Eq. (28) is evaluated for the mode shape:

$$\begin{aligned} \phi(x) &= \left[\mathbf{\Phi}(x,0)\right]_{3,2} N(0) + \left[\mathbf{\Phi}(x,0)\right]_{3,5} M(0) + \left[\mathbf{\Phi}(x,0)\right]_{3,6} V(0) \\ &= \left\{ -\left[\mathbf{\Phi}(x,0)\right]_{3,2} (k_1 + k_2\sigma) + \left[\mathbf{\Phi}(x,0)\right]_{3,5} + \left[\mathbf{\Phi}(x,0)\right]_{3,6} \sigma \right\} M(0) \end{aligned} \tag{29}$$

where the constants are computed according to the following conditions:

case $U_{5,2} \neq 0$:

$$k_1 = \frac{U_{5,5}}{U_{5,2}},\ k_2 = \frac{U_{5,6}}{U_{5,2}}, \text{ and } \sigma = \frac{U_{6,2}U_{5,5} - U_{6,5}U_{5,2}}{U_{6,6}U_{5,2} - U_{6,2}U_{5,6}} \tag{30a}$$

case $U_{6,2} \neq 0$:

$$k_1 = \frac{U_{6,5}}{U_{6,2}},\ k_2 = \frac{U_{6,6}}{U_{6,2}}, \text{ and } \sigma = \frac{U_{6,2}U_{5,5} - U_{6,5}U_{5,2}}{U_{6,6}U_{5,2} - U_{6,2}U_{5,6}} \tag{30b}$$

case $U_{5,2} = 0$ and $U_{6,2} = 0$:

$$k_1 = 0,\ k_2 = 0, \text{ and } \sigma = -\frac{U_{6,5}}{U_{6,6}} \tag{30c}$$

In Eq. (29), the scaling factor $M(0)$ is not retained: instead the mode shapes are scaled in order to satisfy the appropriate orthogonality conditions, as discussed in section 4.2.

4. Solution to electromechanical EOMs via modal analysis

4.1 Calculation of base excitation contribution

In this section, the EOMs are solved using a modal decoupling procedure. However, before this can be accomplished, the external forcing term $f(x,t)$ appearing in Eq. (10) must be evaluated. This term represents an applied transverse force/length along the beam segments. A common use for this term is pressure loads due to flowing media into which the structure is immersed. In the present scenario, this load is the apparent inertial loading due to the excitation of the base in the vertical direction.

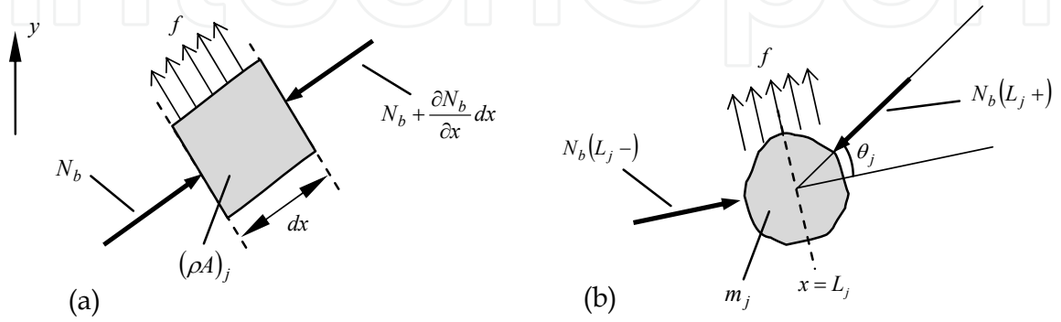

Fig. 4. Forces due to base excitation on a beam element (a) and on a lumped mass located at $x = L_j$ (b).

In Fig. 4, the forces due to the apparent inertial loads from the base excitation are shown for an arbitrary element of a beam segment and a lumped mass. Due to rotations at the lumped mass interfaces, the inertial loads are not strictly transverse or axial, but have components in both directions. The absolute orientation of each component determines how the base excitation affects it; this orientation is the sum of the relative angles between the joints between the base and the component. Only the normal force due to base excitation, denoted N_b, is included here; the other forces and moments have already been accounted for in section 2.2.

A balance of forces in the transverse and axial directions for the element shown in Fig. 4(a) gives

$$f(x,t) = -(\rho A)_j \cos\left(\sum_{i=0}^{j-1} \theta_i\right) \frac{d^2 y(t)}{dt^2} \tag{31}$$

$$\text{and } \frac{\partial N_b(x,t)}{\partial x} = (\rho A)_j \sin\left(\sum_{i=0}^{j-1} \theta_i\right) \frac{d^2 y(t)}{dt^2} \tag{32}$$

respectively, where $\theta_0 \equiv 0$. Eq. (32) can be integrated to get

$$N_b(L_j -) - N_b(L_{j-1} +) = (\rho A)_j l_j \sin\left(\sum_{i=0}^{j-1} \theta_i\right) \frac{d^2 y(t)}{dt^2} \tag{33}$$

Similarly, a balance of forces in the transverse and axial directions for the lumped mass shown in Fig. 4(b) gives

$$f(x,t)=\left[-m_j\cos\left(\sum_{i=0}^{j-1}\theta_i\right)\frac{d^2y(t)}{dt^2}+N_b\left(L_j+\right)\sin\theta_j\right]\delta\left(x-L_j\right) \tag{34}$$

$$\text{and } N_b\left(L_j-\right)-N_b\left(L_j+\right)\cos\theta_j=-m_j\sin\left(\sum_{i=0}^{j-1}\theta_i\right)\frac{d^2y(t)}{dt^2} \tag{35}$$

respectively. Combining Eqs. (31,34) gives

$$\begin{aligned}f(x,t)=&-\frac{d^2y(t)}{dt^2}\sum_{j=1}^{n}\left(\left\{(\rho A)_j\left[H\left(x-L_{j-1}\right)-H\left(x-L_j\right)\right]+m_j\delta\left(x-L_j\right)\right\}\cos\left(\sum_{i=0}^{j-1}\theta_i\right)\right)\\&+N_b\left(L_j+\right)\sin\theta_j\delta\left(x-L_j\right)\end{aligned} \tag{36}$$

where

$$N_b\left(L_n+\right)=0 \text{ and}$$

$$N_b\left(L_j+\right)=-\left[(\rho A)_{j+1}l_{j+1}+m_{j+1}\right]\sin\left(\sum_{i=0}^{j}\theta_i\right)\frac{d^2y(t)}{dt^2}+N_b\left(L_{j+1}+\right)\cos\theta_{j+1} \tag{37}$$

which can be evaluated inductively.

4.2 Modal decoupling

The EOMs for a single beam segment have been derived in section 2.2 and subsequently used to develop the field transfer matrix for such a segment. Using the transfer matrix method, the natural frequencies and mode shapes have been calculated. Now, the time response is found by decoupling the partial differential equations into a system of ordinary differential equations, one for each mode. By concatenating Eq. (10-11) for each segment, the following EOMs, which apply over the entire structure, can be found:

$$\begin{aligned}\sum_{j=1}^{n}\Bigg\{&\left[(\rho A)_j\frac{\partial^2w(x,t)}{\partial t^2}+(EI)_j\frac{\partial^4w(x,t)}{\partial x^4}\right]\left[H\left(x-L_{j-1}\right)-H\left(x-L_j\right)\right]+\\&+\vartheta_j\left[\frac{d\delta\left(x-L_L\right)}{dx}-\frac{d\delta\left(x-L_R\right)}{dx}\right]v(t)\Bigg\}=f(x,t)\end{aligned} \tag{38}$$

$$q(t)=\sum_{j=1}^{n}\vartheta_j\left[\left.\frac{\partial w(x,t)}{\partial x}\right|_{x=L_R}-\left.\frac{\partial w(x,t)}{\partial x}\right|_{x=L_L}\right]-\sum_{j=1}^{n}C_jv(t) \tag{39}$$

where the external forcing due to base excitation can be evaluated using Eq. (36).

To orthonormalize the mode shapes, Eq. (38) is considered when there are no external loads (including electrical), i.e. $v(t)\equiv 0$ and $f(x,t)\equiv 0$. Substituting the modal decomposition given by Eq. (1), and assuming a sinusoidal time response gives

$$\omega_r^2 \sum_{j=1}^{n} \left\{ \left[(\rho A)_j \phi_r(x) \right] \left[H\left(x - L_{j-1}\right) - H\left(x - L_j\right) \right] \right\} = \sum_{j=1}^{n} \left\{ \left[(EI)_j \frac{d^4 \phi_r(x)}{dx^4} \right] \left[H\left(x - L_{j-1}\right) - H\left(x - L_j\right) \right] \right\} \quad (40)$$

for each term *r* in the modal expansion. Subsequently, Eq. (40) is multiplied by $\phi_s(x)$ and integrated from $x = 0$ to $x = L_n$. After integrating by parts and applying the boundary and intermediate conditions (i.e. across the lumped masses), the following orthogonality condition is derived:

$$\sum_{j=1}^{n} \left[\int_{L_{j-1}}^{L_j} (\rho A)_j \phi_r(x) \phi_s(x) dx + m_j \phi_r\left(L_j -\right) \phi_s\left(L_j -\right) + I_j \left. \frac{d\phi_r(x)}{dx} \right|_{x=L_j -} \left. \frac{d\phi_s(x)}{dx} \right|_{x=L_j -} + (\rho A)_j l_j \psi_r\left(L_j -\right) \psi_s\left(L_j -\right) + m_j \psi_r\left(L_j -\right) \psi_s\left(L_j -\right) \right] = \delta_{rs} \quad (41)$$

where δ_{rs} is the Kronecker delta. If the mode shapes are scaled appropriately such that Eq. (41) is satisfied, then automatically

$$\sum_{j=1}^{n} (EI)_j \left[\int_{L_{j-1}}^{L_j} \frac{d^4 \phi_r(x)}{dx^4} \phi_s(x) dx - \left. \frac{d^3 \phi_r(x)}{dx^3} \right|_{x=L_j -} \left. \frac{d\phi_s(x)}{dx} \right|_{x=L_j -} + \left. \frac{d^3 \phi_r(x)}{dx^3} \right|_{x=L_{j-1}+} \left. \frac{d\phi_s(x)}{dx} \right|_{x=L_{j-1}+} + \left. \frac{d^2 \phi_r(x)}{dx^2} \right|_{x=L_j -} \left. \frac{d\phi_s(x)}{dx} \right|_{x=L_j -} - \left. \frac{d\phi_r(x)}{dx} \right|_{x=L_{j-1}+} \left. \frac{d\phi_s(x)}{dx} \right|_{x=L_{j-1}+} \right] = \omega_r^2 \delta_{rs} \quad (42)$$

is satisfied, thus decoupling Eq. (38). Subsequently, the natural frequencies and mode shape functions derived from the TMM can be adopted into existing piezoelectric energy harvester models for evaluating continuous and discontinuous structures.

4.3 Frequency response functions

Once the EOMs are decoupled by mode, the frequency response functions (FRFs) of the structure can be obtained in a straightforward manner by substituting the modal expansions given by Eq. (1) into Eq. (38-39) and applying the orthogonality conditions of Eqs. (41-42). The decoupled forms of Eqs. (38-39) are given for the *r*th mode:

$$\frac{d^2 \eta_r(t)}{dt^2} + 2\zeta_r \omega_r \frac{d\eta_r(t)}{dt} + \omega_r^2 \eta_r(t) + \Theta_r v(t) = -(\rho A \gamma)_r \frac{d^2 y(t)}{dt^2} \quad (43)$$

$$\frac{dv(t)}{dt} + \frac{1}{R_l C_0} v(t) = \frac{1}{C_0} \sum_{r=1}^{\infty} \Theta_r \frac{d\eta_r(t)}{dt} \quad (44)$$

where Eq. (43) represents the mechanical equation, in which the modal short-circuit frequencies ω_r are equal to the natural frequencies derived from the TMM. (Setting $v(t) \equiv 0$,

i.e. shorting the terminals of the device, is equivalent to decoupling the electrical from the mechanical dynamics.) The modal electromechanical coupling is given by

$$\Theta_r = \sum_{j=1}^{n} \vartheta_j \left[\left. \frac{d\phi_r(x)}{dx} \right|_{x=L_j} - \left. \frac{d\phi_r(x)}{dx} \right|_{x=L_{j-1}} \right] \tag{45}$$

and the modal influence coefficient of the distributed inertial force along the beam is

$$(\rho A\gamma)_r = \sum_{j=1}^{n} \left\{ \left[\int_{L_{j-1}}^{L_j} (\rho A)_j \phi_r(x) dx + m_j \phi_r(L_j -) \right] \cos\left(\sum_{i=0}^{j-1} \theta_i \right) + N_b(L_j +) \sin\theta_j \phi_r(L_j -) \right\} \tag{46}$$

Note that the modal damping term $2\zeta_r \omega_r (d\eta_r(t)/dt)$ has been added at this point, although the value of the modal damping ratio is usually determined experimentally.

Eq. (44) represents the electrical dynamics equation where the terminals of the device are assumed to be placed across an external resistor R_l. The net clamped, i.e. constant strain, capacitance of the piezoelectric material, appearing in Eq. (44), is defined as

$$C_0 = \sum_{j=1}^{n} C_j \tag{47}$$

which in the parallel bimorph configuration is simply the sum of the capacitances of the beam segments. On the right-hand side of Eq. (44), the same Θ_r appearing in Eq. (43) is used to couple the two modal EOMs. It should be noted that only under mass-normalized conditions, i.e. Eq. (41), are these two coupling coefficients equal.

To evaluate the FRFs of the structure, a harmonic base excitation $y(t) = Ye^{i\omega t}$ is assumed. Given that the eigensolutions are derived from Euler-Bernoulli beam theory (resulting in a linear PDE), and the piezoelectric constitutive equations are also linearized (see Eq. (8)), the resulting motion and voltage output are also harmonic at the base excitation frequency. Thus, the relative transverse motion at a point x from the base is given by

$$w(x,t) = W(x)e^{i\omega t} = \sum_{r=1}^{\infty} \frac{(\rho A\gamma)_r \omega^2 Y - \Theta_r V}{\omega_r^2 - \omega^2 + i2\zeta_r \omega_r \omega} \phi_r(x) e^{i\omega t} \tag{48}$$

where $i = \sqrt{-1}$, and the voltage output is

$$v(t) = Ve^{i\omega t} = \frac{\frac{1}{C_0} \sum_{r=1}^{\infty} \frac{i(\rho A\gamma)_r \omega^3 \Theta_r Y}{\omega_r^2 - \omega^2 + i2\zeta_r \omega_r \omega}}{i\omega + \frac{1}{R_l C_0} + \frac{1}{C_0} \sum_{r=1}^{\infty} \frac{i\omega {\Theta_r}^2}{\omega_r^2 - \omega^2 + i2\zeta_r \omega_r \omega}} e^{i\omega t} \tag{49}$$

Finally, the current output of the device can be found from $i(t) = v(t)/R_l$ and the power from $p(t) = [v(t)]^2 / R_l$.

5. Case studies

In order to demonstrate the use of the TMM for analysis of multi-segmented beam structures, a few simple examples are given. Fig. 5 depicts the two cases under consideration. Fig. 5(a) shows a bimorph beam with varying piezoelectric layer coverage starting from the base and extending to the point x_{div}, the dividing line between the two segments. Note that the point transfer matrix between the two segments, given in Eq. (24), reduces to the identity matrix in this case. Fig. 5(b) shows a bimorph beam with varying center joint angle. The special case $\theta_1 = 0^\circ$ corresponds to a standard cantilevered bimorph, whereas the case $\theta_1 = 90^\circ$ corresponds to an L-shaped structure, previously studied by (Erturk et al., 2009). In both cases, the overall length of the structure is kept constant. The geometry and material properties of the device are listed in Table 1.

Fig. 6 plots the variation in fundamental (short-circuit) natural frequency as x_{div} is varied between 0 and L, the overall length of the structure, and the layer thickness ratio (over the segment with piezoelectric coverage) is varied between $t_p/t_s = 0.05$ and $t_p/t_s = 3$. These curves indicate that in each case the beam with full coverage has a higher natural frequency than the beam with no coverage, with agrees with the fact that the effective stiffness increases when the piezoelectric layers are added, i.e. $(EI)_1 > (EI)_2$. Furthermore, this effect is exacerbated with larger layer thickness ratio. Somewhat surprisingly, the natural frequency has a maximum at a point of partial coverage; this maximum shifts towards $x_{div} = L$ as t_p/t_s increases. This phenomenon can be explained by considering that the partial coverage makes the beam effectively shorter, since the bare substructure section does not contribute to the stiffness as significantly. Increasing the layer coverage past this maximum effectively lengthens the beam, thus decreasing its natural frequency. The reverse effect occurs as the layer coverage decreases further: the bare substructure region dominates, reducing the natural frequency.

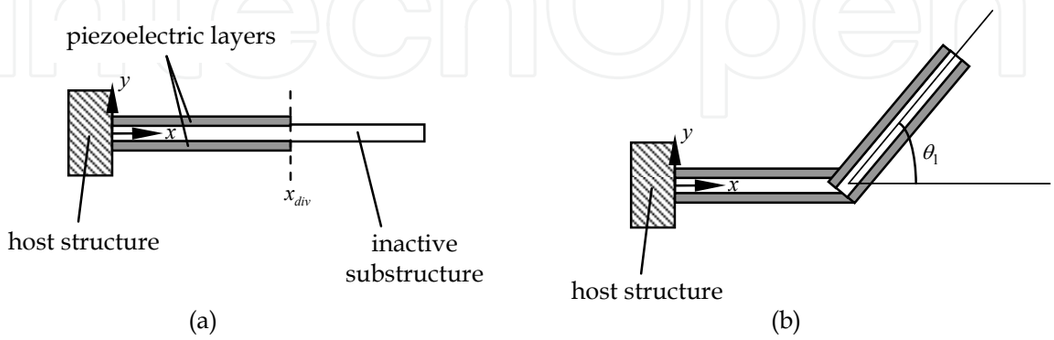

Fig. 5. (a) Layout of bimorph structure with partial piezoelectric layer coverage. (b) Layout of bimorph structure with a variable-angle bend at half its overall length.

Beam properties:		
L	length	100 mm
b	width	20 mm
t_s	thickness of substructure	0.75 mm
t_p	thickness of PZT layer	0.5 mm
ρ_s	density of substructure	8070 kg/m^3
ρ_p	density of PZT	7800 kg/m^3
$c_{11.s}$	Young's modulus of substructure	102 GPa
c_{11}^E	Young's modulus of PZT	66 GPa
e_{31}	piezoelectric constant	-12.54 C/m^2
ε_{33}^S	permittivity	15.93 nF/m

Table 1. Geometry and material properties.

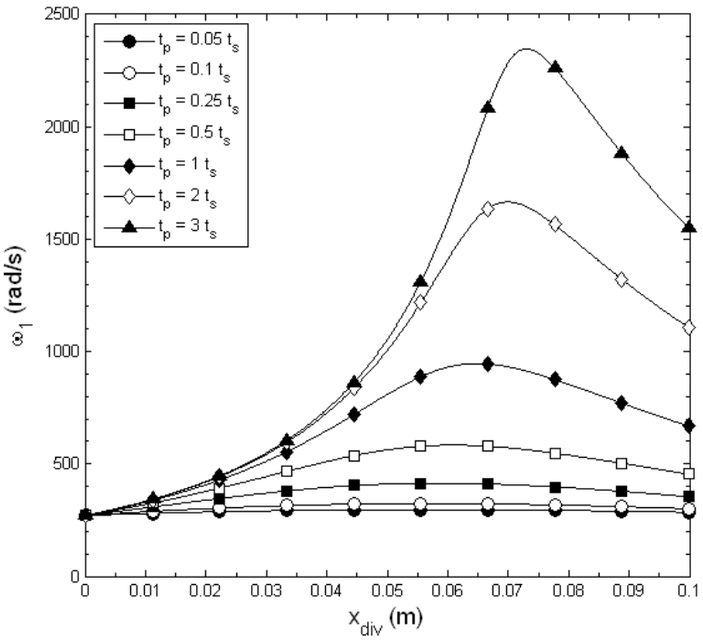

Fig. 6. Variation in fundamental (short-circuit) natural frequency with respect to patch coverage and layer thickness ratio.

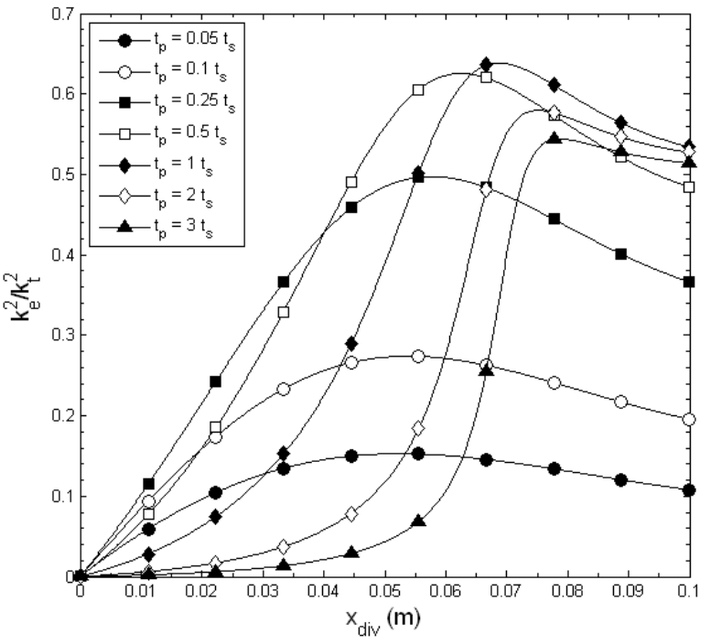

Fig. 7. Variation in coupling coefficient ratio with respect to patch coverage and layer thickness ratio.

To quantify the effects on the transduction capabilities of these two designs, the dimensionless electromechanical coupling coefficient is employed. The device (i.e. entire structure) coupling coefficient for the r^{th} mode is given by $k_e^2 = \Theta_r^2 \Big/ \left(C_0 \omega_r^2 \right)$, a term that has been used to non-dimensionalize power in the literature, e.g. (Shu and Lien, 2006; Liao and Sodano, 2008; Wickenheiser and Garcia, 2010c). It has been shown by (Wickenheiser, 2011) that this term can be written in the form

$$k_e^2 = k_t^2 \kappa_M \kappa_{EI} \tag{50}$$

for single segment beams (with or without tip mass), where $k_t^2 = e_{31}^2 \Big/ \left(c_{11}^E \varepsilon_{33}^S \right)$ is the piezoelectric material coupling coefficient, κ_M is a dimensionless term that depends on the distribution of inertia between the beam and tip mass, and κ_{EI} is a dimensionless term that depends on the effective stiffness of the beam. Although the simple decomposition of Eq. (50) is not proven for more general structures, it can be shown that the ratio k_e^2 / k_t^2 is constant for a specific geometry.

In the present study, the ratio k_e^2 / k_t^2 is plotted, isolating the effects of geometry on the electromechanical coupling of the device. In Fig. 7, the piezoelectric layers are extended out from the base to x_{div}. As the coverage decreases to 0, $k_e^2 / k_t^2 \to 0$ as expected. As it increases, there is a maximum before $x_{div} = L$, similar to Fig. 6. This indicates that the extra coverage at the end of the beam is not utilized efficiently, which is due to the relative lack of strain there. Furthermore, increasing the piezoelectric layer thickness does not result in increased coupling past a certain point; this phenomenon is explored in more detail in (Wickenheiser, 2011). Briefly, the increased thickness increases the stiffness more quickly than the dimensional coupling coefficient, resulting in decreased k_e^2.

Figs. 8-10 show the results of the center joint angle parameter study for the design depicted in Fig. 5(b). In this study, the center joint angle θ_1 is varied between 0 and 180 deg. Both beam segments are identical bimorphs. As with the previous case, increasing the piezoelectric layer thickness increases the bending stiffness and therefore the natural frequencies, as shown in Fig. 8. This plot also indicates that the fundamental frequency increases with center joint angle, which causes an effective shortening of the beam. Fig. 9 shows the variation in the ratio of the first two natural frequencies ω_2/ω_1. First, these results indicate that this ratio is independent of the thickness ratio of the layers; this result is confirmed by (Wickenheiser, 2011), who shows that this ratio is only a function of the ratio of non-dimensional eigenvalues of the device. Moreover, as the device is folded back on itself, i.e. θ_1 increases, the first natural frequency increases while the second decreases, both converging to a common value. As mentioned by (Erturk et al., 2009), this convergence is useful for broadband energy harvesting from a range of excitation frequencies between these two natural frequencies. Furthermore, energy exchange between modes becomes possible when the natural frequencies are commensurable (Nayfeh and Mook, 1979), a useful mechanism for exciting a higher frequency mode from a lower frequency excitation. Finally, Fig. 10 indicates that the coupling coefficient is relatively insensitive to center join angle. This insensitivity is mainly due to the small impact on the strain at the root, where most of the energy is harvested, by the rotation of the relatively strain-free tip segment.

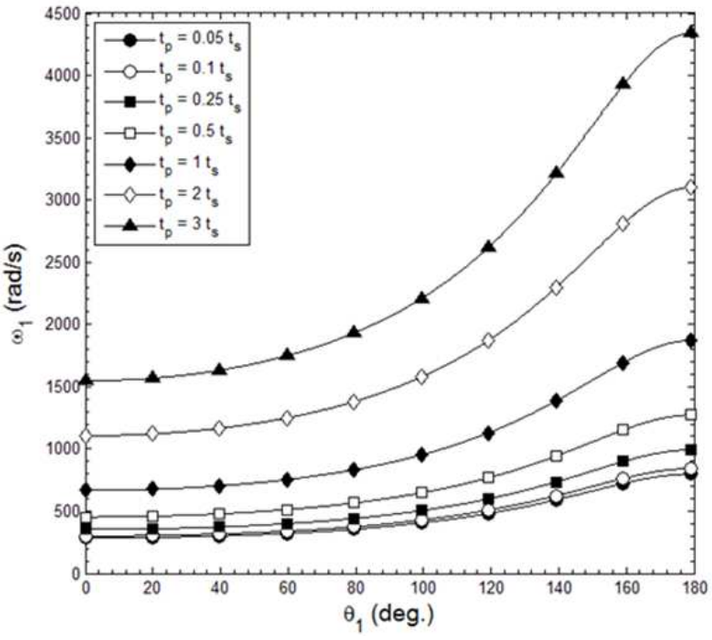

Fig. 8. Variation in fundamental (short-circuit) natural frequency with respect to center joint angle and layer thickness ratio.

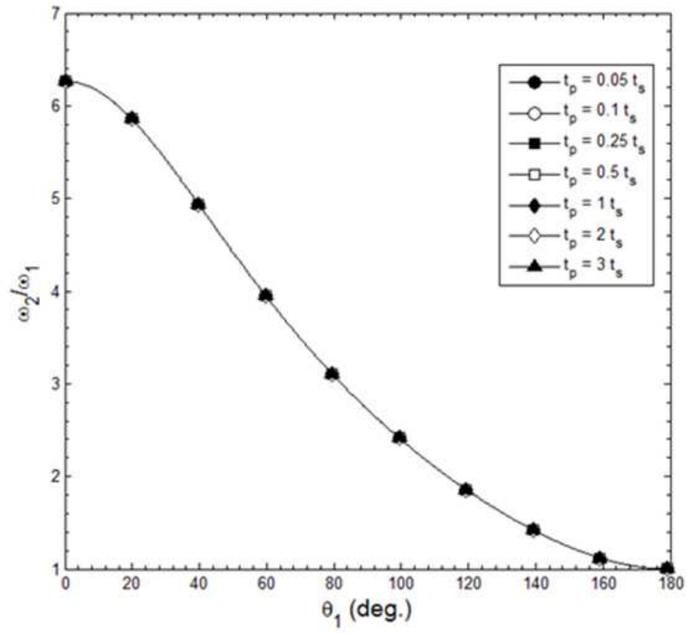

Fig. 9. Variation in ratio of first two natural frequencies with respect to center joint angle and layer thickness ratio.

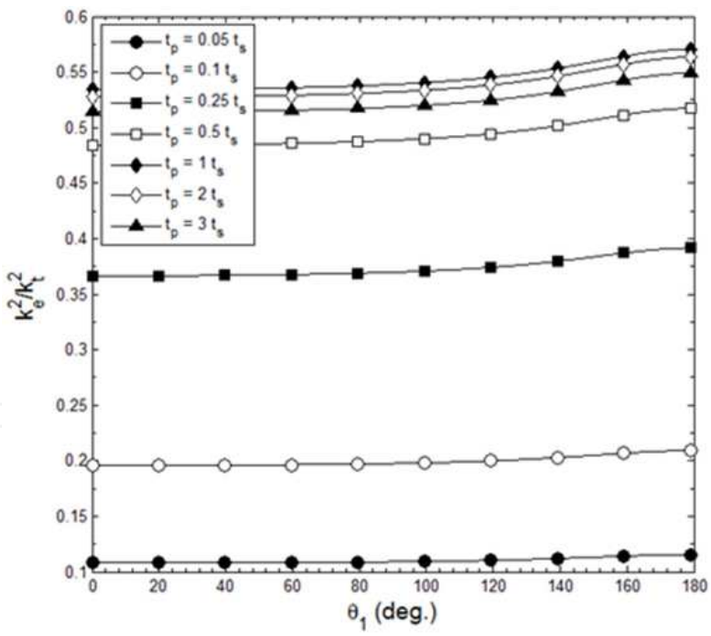

Fig. 10. Variation in coupling coefficient ratio with respect to center joint angle and layer thickness ratio.

6. Conclusions

This chapter presents an electromechanical modeling technique for computing the eigensolution and frequency transfer functions for segmented beams using the transfer

matrix method. This method allows for multiple discontinuities in the beam structure, for example partial layer coverage, discontinuities in cross section, angles between members, and multiple lumped masses along the length. The electromechanical equations of motion, including distributed inertial effects from the base excitation, are derived in general terms for various piezoelectric layering configurations. Transfer matrices are derived for each continuous segment and each discontinuity, and a system transfer function is described using the semigroup property of state transition matrices.

This method is general enough to be effective at analyzing many configurations of piezoelectric structures without requiring a re-derivation starting from first principles. Axial and transverse dynamics are shown to be decoupled, leading to block diagonal transfer matrices. Furthermore, it is shown that the size of the eigenvalue problem does not grow with added complexity to the structure, unlike finite element methods. In this chapter, this method is applied to structures with partial piezoelectric layer coverage, taking into account the discontinuity in cross section at the end of the piezoelectric layers. Additionally, variations in center angle are discussed, including the special cases of L-shaped and reflex beams. The natural frequencies and electromechanical coupling coefficients are computed and discussed, displaying the usefulness and versatility of this technique in the design and analysis of complex structures.

7. References

(1987). *IEEE Standard on Piezoelectricity,* IEEE, New York, NY.

Anton, S. R. & Sodano, H. A. (2007). A review of power harvesting using piezoelectric materials (2003–2006). *Smart Materials and Structures,* Vol.6, No.3, (June 2007), pp. R1–R21, ISSN 0964-1726.

Beer, F. P. & Johnson, Jr. E. R. (1992). *Mechanics of Materials* (2nd), McGraw-Hill, ISBN 0-07-004340-X, New York, NY.

Dietl, J. M. & Garcia, E. (2010). Beam shape optimization for power harvesting. *Journal of Intelligent Material Systems and Structures*, Vol.21, pp. 633–646, ISSN 1045389X.

duToit N. E., Wardle, B. L. & Kim, S. (2005). Design Considerations for MEMS-Scale Piezoelectric Mechanical Vibrations Energy Harvesting. *Integrated Ferroelectrics*, Vol.71, pp. 121–160, ISSN 1058-4587.

Erturk, A. & Inman, D. J. (2008). A Distributed Parameter Electromechanical Model for Cantilevered Piezoelectric Energy Harvesters. *Journal of Vibrations and Acoustics*, Vol.130, No.4, 041002, ISSN 10489002.

Erturk, A.; Renno, J. M. & Inman, D.J. (2009). Modeling of piezoelectric energy harvesting from an L-shaped beam-mass structure with an application to UAVs. *Journal of Intelligent Materials Systems and Structures*, Vol.20, pp. 529–544, ISSN 1045-389X.

Guyomar, D.; Badel, A.; Lefeuvre, E. & Richard, C. (2005). Toward energy harvesting using active materials and conversion improvement by nonlinear processing. *IEEE Transactions on Ultrasonics, Ferroelectrics, and Frequency Control*, Vol.52, No.4, (April 2005), pp. 584–595, ISSN 08853010.

Inman, D. J. (2007). *Engineering Vibration* (3rd), Pearson, ISBN 0-13-228173-2, Upper Saddle River, NJ.

Karami, M. A. & Inman, D. J. (2011). Electromechanical Modeling of the Low-Frequency Zigzag Micro-Energy Harvester. *Journal of Intelligent Material Systems and Structures*, Vol.22, No. 3, pp. 271–282, ISSN 1045389X.

Liao, Y. & Sodano, H. A. (2008). Model of a single mode energy harvester and properties for optimal power generation. *Smart Materials and Structures*, Vol.17, No.6, 065026, ISSN 09641726.

Murray, R. & Rastegar, J. (2009). Novel Two-Stage Piezoelectric-Based Ocean Wave Energy Harvesters for Moored or Unmoored Buoys. *Proceedings of SPIE*, ISSN 0277-786X, San Diego, CA, March, 2009.

Nayfeh, A. H. & Mook, D. T. (1979). *Nonlinear Oscillations*, Wiley, ISBN 0471121428, New York, NY.

Pestel, E. & Leckie, F. A. (1963). *Matrix Methods in Elastomechanics*, McGraw-Hill, ASIN B000BLO2YI, New York, NY.

Reissman, T.; Dietl, J. M. & Garcia, E. (2007). Modeling and Experimental Verification of Geometry Effects on Piezoelectric Energy Harvesters. *Proceedings of 3rd Annual Energy Harvesting Workshop*, Santa Fe, NM, February, 2007.

Reissman, T., Wickenheiser, A. M. & Garcia, E. (2011) Closed Form Solutions for the Dynamic Response of Piezoelectric Energy Harvesting Structures with Non-Uniform Geometries. (in preparation).

Roundy, S.; Leland, E. S.; Baker, J.; Carleton, E.; Reilly, E.; Lai, E.; Otis, B.; Rabaey, J.M.; Wright, P.K. & Sundararajan, V. (2005). Improving power output for vibration-based energy scavengers. *Pervasive Computing*, Vol.4, No.1, pp. 28–36, ISSN 1526-1268.

Roundy, S. & Wright, P. K. (2004). A piezoelectric vibration based generator for wireless electronics. *Smart Materials and Structures*, Vol.13, No.5, pp. 1131–1142, ISSN 09641726.

Roundy, S.; Wright, P. K. & Rabaey, J. (2003). A study of low level vibrations as a power source for wireless sensor nodes. *Computer Communications*, Vol.26, No.11, pp.1131–1144, ISSN 0140-3664.

Sodano, H. A., Park, G. & Inman, D. J. (2004). Estimation of Electric Charge Output for Piezoelectric Energy Harvesting. *Strain*, Vol.40, No.2, pp. 49–58, ISSN 00392103.

Shu, Y. C. & Lien, I. C. (2006). Analysis of power output for piezoelectric energy harvesting systems. *Smart Materials and Structures*, Vol.15, No.6, pp. 1499–1512, ISSN 0964-1726.

Tieck, R. M.; Carman, G. P. & Lee, D. G. E. (2006). Electrical Energy Harvesting Using a Mechanical Rectification Approach. *Proceedings of IMECE*, pp. 547–553, ISBN 0791837904.

Wickenheiser, A. M. (2011). Design Optimization of Linear and Nonlinear Cantilevered Energy Harvesters for Broadband Vibrations. *Journal of Intelligent Material Systems and Structures*, Vol. 22, No. 11, pp. 1213-1225, ISSN 1045389X.

Wickenheiser, A. & Garcia, E. (2010a). Design of energy harvesting systems for harnessing vibrational motion from human and vehicular motion. *Proceedings of SPIE*, ISSN 0277-786X, San Diego, CA, March, 2010.

Wickenheiser, A. M. & Garcia, E., (2010b). Broadband vibration-based energy harvesting improvement through frequency up-conversion by magnetic excitation. *Smart Materials and Structures*, Vol.19, No.6, 065020, ISSN 09641726.

Wickenheiser, A. M. & Garcia, E. (2010c). Power Optimization of Vibration Energy Harvesters Utilizing Passive and Active Circuits. *Journal of Intelligent Materials Systems and Structures*, Vol.21, No.13, pp. 1343–1361, ISSN 1045389X.

Wu, W. J., Wickenheiser, A. M., Reissman, T. & Garcia, E. (2009). Modeling and experimental verification of synchronized discharging techniques for boosting power harvesting from piezoelectric transducers. *Smart Materials and Structures*, Vol.18, No.5, 055012, ISSN 0964-1726.

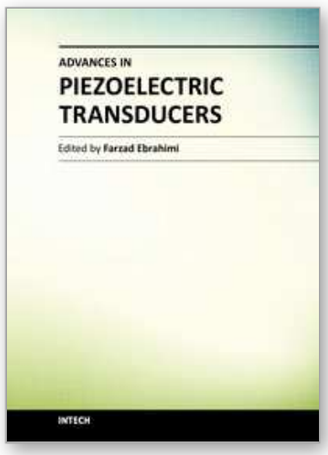

Advances in Piezoelectric Transducers

Edited by Dr. Farzad Ebrahimi

ISBN 978-953-307-931-8
Hard cover, 128 pages
Publisher InTech
Published online 25, November, 2011
Published in print edition November, 2011

The piezoelectric transducer converts electric signals into mechanical vibrations or vice versa by utilizing the morphological change of a crystal which occurs on voltage application, or conversely by monitoring the voltage generated by a pressure applied on a crystal. This book reports on the state of the art research and development findings on this very broad matter through original and innovative research studies exhibiting various investigation directions. The present book is a result of contributions of experts from international scientific community working in different aspects of piezoelectric transducers. The text is addressed not only to researchers, but also to professional engineers, students and other experts in a variety of disciplines, both academic and industrial seeking to gain a better understanding of what has been done in the field recently, and what kind of open problems are in this area.

INTECH
open science | open minds

InTech Europe
University Campus STeP Ri
Slavka Krautzeka 83/A
51000 Rijeka, Croatia
Phone: +385 (51) 770 447
Fax: +385 (51) 686 166
www.intechopen.com

InTech China
Unit 405, Office Block, Hotel Equatorial Shanghai
No.65, Yan An Road (West), Shanghai, 200040, China
中国上海市延安西路65号上海国际贵都大饭店办公楼405单元
Phone: +86-21-62489820
Fax: +86-21-62489821

IntechOpen